OPEN ACCESS
IOP Publishing
Journal of Physics D: Applied Physics
J. Phys. D: Appl. Phys. **54** (2021) 035302 (12pp)
https://doi.org/10.1088/1361-6463/abbc95

A systematic comparison of polar and semipolar Si-doped AlGaN alloys with high AlN content

Lucia Spasevski[1], Gunnar Kusch[1,2], Pietro Pampili[3,4], Vitaly Z Zubialevich[3], Duc V Dinh[3,5], Jochen Bruckbauer[1], Paul R Edwards[1], Peter J Parbrook[3,4] and Robert W Martin[1]

[1] Department of Physics, Scottish Universities Physics Alliance, University of Strathclyde, Glasgow G4 0NG, United Kingdom
[2] Current address: Department of Materials Science and Metallurgy, University of Cambridge, Cambridge CB3 0FS, United Kingdom
[3] Tyndall National Institute, University College Cork, Cork T12 R5CP, Ireland
[4] School of Engineering, University College Cork, T12 K8AF, Ireland
[5] Current address: Institute of Materials and Systems for Sustainability, Nagoya University, Nagoya 464-8601, Japan

E-mail: lucia.spasevski@strath.ac.uk and r.w.martin@strath.ac.uk

Received 1 July 2020, revised 11 September 2020
Accepted for publication 29 September 2020
Published 22 October 2020

Abstract

With a view to supporting the development of ultra-violet light-emitting diodes and related devices, the compositional, emission and morphology properties of Si-doped *n*-type $Al_xGa_{1-x}N$ alloys are extensively compared. This study has been designed to determine how the different $Al_xGa_{1-x}N$ crystal orientations (polar (0001) and semipolar (11–22)) affect group-III composition and Si incorporation. Wavelength dispersive x-ray (WDX) spectroscopy was used to determine the AlN mole fraction ($x \approx 0.57$–0.85) and dopant concentration (3×10^{18}–1×10^{19} cm^{-3}) in various series of $Al_xGa_{1-x}N$ layers grown on (0001) and (11–22) AlN/sapphire templates by metalorganic chemical vapor deposition. The polar samples exhibit hexagonal surface features with Ga-rich boundaries confirmed by WDX mapping. Surface morphology was examined by atomic force microscopy for samples grown with different disilane flow rates and the semipolar samples were shown to have smoother surfaces than their polar counterparts, with an approximate 15% reduction in roughness. Optical characterization using cathodoluminescence (CL) spectroscopy allowed analysis of near-band edge emission in the range 4.0–5.4 eV as well as various deep impurity transition peaks in the range 2.7–4.8 eV. The combination of spatially-resolved characterization techniques, including CL and WDX, has provided detailed information on how the crystal growth direction affects the alloy and dopant concentrations.

Keywords: AlGaN, crystal orientation, alloy composition, III-nitride semiconductors, Si doping, cathodoluminescence, x-ray microanalysis

(Some figures may appear in colour only in the online journal)

1. Introduction

$Al_xGa_{1-x}N$ is a promising material for optoelectronic devices such as ultraviolet (UV) light-emitting diodes (LEDs) and laser diodes operating in the wavelength range from 210 to 365 nm, depending on the AlN mole fraction x [1–3]. It is also possible to control $Al_xGa_{1-x}N$ properties such as spontaneous and piezoelectric polarization constants, and lattice constants through group-III compositions in order to obtain the optimal characteristics for the target nitride devices [4]. Most $Al_xGa_{1-x}N$ layers are grown on sapphire substrates due to limited availability of native AlN substrates (generally only with small diameters, typically about 1″, and at very high cost). Heteroepitaxy on sapphire substrates usually results in growth of $Al_xGa_{1-x}N$ layers with high threading dislocation densities due to the lattice and thermal expansion coefficient mismatches [5, 6]. These are significant challenges for the production of high quality AlN-rich $Al_xGa_{1-x}N$ films needed for devices [2]. $Al_xGa_{1-x}N$-based LEDs have attracted a lot of attention, with a view to increasing the low emission efficiencies for devices emitting below 300 nm [3]. This lower emission efficiency is a result of various factors, including high dislocation densities, high resistivity and poor light extraction efficiency [7]. $Al_xGa_{1-x}N$-based deep-ultraviolet (DUV) LED bare dies with external quantum efficiencies (EQEs) of 3.5% at 265 nm, over 4.5% at 270 nm, and over 6% between 280 nm and 300 nm without encapsulation and with a *p*-GaN contact layer have been reported [7, 8]. However, for LEDs emitting around 250 nm, EQEs remain around 2% [1]. One of the major requirements for the device fabrication is successful doping with Si, which is the most common donor for *n*-type $Al_xGa_{1-x}N$ layers [9, 10]. The Si doping changes the structural, electrical and optical properties of the $Al_xGa_{1-x}N$ material. The main changes are in electric conductivity [11], but there are also changes in luminescence efficiency [12], optical polarization [13], point defect-density [13, 14], and mechanical strain [15], particularly through the phenomenon of dislocation inclination [16]. As the AlN fraction increases above 0.8 it becomes increasingly challenging to obtain high conductivity [10, 17]. This effect arises from the self-compensation effects of the Si donor and from a transition of Si from a shallow donor to a DX center [18, 19]. In turn this leads to an increase in activation energy E_A of Si with increasing AlN fraction [10, 17]. Other factors that influence carrier compensation in the $Al_xGa_{1-x}N$ material are threading dislocations, unintentional impurities and native defects [20].

Trap states introduced by defects in the bandgap often reduce the electrical conductivity [21]. They can be associated with specific luminescence peaks from AlGaN, making it possible to use the cathodoluminescence (CL) spectroscopy employed in this work to confirm the existence of different defects. A range of defects are present in AlGaN, including cation vacancies $(V_{III})^{3-}$ and defect complexes comprising the cation vacancy plus oxygen, with either one or two negative charges. These defects have small formation energies in AlN-rich AlGaN and are easily formed in undoped and Si-doped AlGaN layers [22]. Mehnke *et al* [23] showed how the drop in the resistivity of AlGaN: Si layers is related to the self-compensation effects that may be attributed to the increasing formation of vacancies or vacancy-oxygen complexes with increasing Al content. It has been confirmed that the increase of the resistivity with increasing Al is mainly caused by a decrease in the carrier density [23, 24]. For the set of samples studied, compensation effects were confirmed for semipolar and polar samples, where for the optimized (A4SP) sample a carrier concentration of $\sim 1.2 \times 10^{19} cm^{-3}$ was measured but on further increase in the Si/III ratio (sample A5SP) the carrier concentration and mobility decreased, indicating the beginning of Si over-compensation [25]. For the polar set of samples, a significant amount of the conductivity was due to phonon-assisted hopping among localized states in the impurity band. Free-carrier concentration in the conduction band has already reached its maximum of 1.6×10^{18} cm^{-3} at a Si/III ratio of 2.8×10^{-5} cm^{-3} (sample A1P) and any further increase of dopant atoms supplied during growth only enhances the impurity-band conduction with concentrations of the carriers participating in this type of transport that increase from 2.1×10^{18} cm^{-3} up to 4.3×10^{18} cm^{-3}. This process eventually stops when a critical Si/III ratio is reached and the band-like channel starts to degrade (i.e. at sample A4P) and above [26].

Using CL to identify the suppression of these vacancy complex defects will lead to further improvements in the conductivity.

In the case of the semipolar AlGaN a minimum resistivity of 0.018 Ωcm was reported for the optimised layer with 60% AlN content (A4SP) [25]. For semipolar AlGaN samples with 60% AlN content Jo *et al* reported resistivity of 0.009 Ωcm [27]. For the polar samples with 60% AlN content the reported resistivity values were much higher, e.g. ∼10 Ωcm for sample A1P [26]. The resistivity in high AlN content AlGaN has been shown to increase steeply from 0.026 Ωcm to 2.62 Ωcm as AlN content increased from 82%–95% [23].

Traditionally, $Al_xGa_{1-x}N$ is grown in the polar (0001) *c*-plane orientation because it is relatively easy to obtain higher material quality in this orientation. The drawback of this orientation is that the corresponding structures suffer from a strong polarization-induced quantum confined Stark effect and exciton localization [28, 29]. Growth in semipolar directions can significantly reduce the polarization-induced electrical fields. Furthermore, exciton localization in semipolar $Al_xGa_{1-x}N$ is significantly reduced compared to *c*-plane $Al_xGa_{1-x}N$ due to a reduction in alloy compositional fluctuations [30, 31]. As a consequence, semipolar $Al_xGa_{1-x}N$ has significant potential in terms of improving the performance of DUV LEDs.

This paper reports on a systematic study of polar and semipolar *n*-type doped $Al_xGa_{1-x}N$:Si/AlN layers grown on sapphire by metalorganic chemical vapor deposition (MOCVD) with varied Si/group-III ratios in the gas phase. High AlN alloy fraction samples were investigated because the difference in the lattice constants between the $Al_xGa_{1-x}N$ and the AlN layer decreases with increasing AlN alloy fraction, reducing the density of misfit dislocations [32]. Systematic reports comparing the optical properties of semipolar and polar $Al_xGa_{1-x}N$

Table 1. Sample series details.

Label	Crystal orientation	$\frac{\text{TMAl}}{\text{TMGa}+\text{TMAl}}$ ratio	Approx. growth rate (nm^{-s})	Si_2H_6/III ratio ($\times 10^{-7}$)	V/III ratio	WDX Si content (10^{18} cm^{-3})	AlN fraction x
A1P				279		4	0.63
A2P				558		4	0.72
A3P	(0001)	0.5	0.23	1120	600	5	0.69
A4P				2230		8	0.63
A5P				3350		10	0.70
A1SP				279		3	0.57
A2SP				558		7	0.65
A3SP	(11–22)	0.5	0.23	1120	600	7	0.61
A4SP				2230		8	0.60
A5SP				3350		6	0.60
B1P				131		3	0.85
B2P				219		5	0.84
B3P	(0001)	0.824	0.66	328	460	10	0.85
B4P				437		4	0.85
B5P				656		5	0.84
C1P				112		3	0.81
C2P				299		5	0.82
C3P	(0001)	0.333	0.31	449	23	4	0.82
C4P				561		4	0.82
C5P				749		6	0.82
C1SP				112		4	0.75
C2SP				299		3	0.78
C3SP	(11–22)	0.333	0.31	449	23	3	0.77
C4SP				561		7	0.75
C5SP				749		3	0.76

materials should be valuable with a view to guiding improvements in material quality.

Wavelength dispersive x-ray (WDX) microanalysis and CL spectroscopy were used to evaluate the doping characteristics and optical properties of a wide range of Si-doped $Al_xGa_{1-x}N$ layers (n-$Al_xGa_{1-x}N$). The samples studied were 0.8–1.1 μm-thick layers with Si concentrations ([Si]) in the range from 2×10^{18} cm^{-3} to 1×10^{19} cm^{-3}, grown along polar (0001) and semipolar (11–22) planes.

2. Experimental

The $Al_xGa_{1-x}N$ films were grown in an Aixtron 3 × 2 inch close-coupled showerhead MOCVD reactor on (0001)- and (11-22)-oriented AlN/sapphire templates for polar and semipolar samples, respectively. The templates were prepared as described in [33] and [34] for polar and semipolar orientations, respectively. Trimethylgallium (TMGa) and trimethylaluminium (TMAl) were used as group-III precursors, and ammonia (NH_3) was used as the nitrogen precursor. H_2 was used as the carrier gas and disilane (Si_2H_6) as the doping source. The AlN fraction was controlled by varying TMAl/(TMGa + TMAl) ratio, V/III ratios and growth rate. Three series of experiments were performed at different growth conditions, varying the Si_2H_6/III ratio while keeping all other parameters nominally fixed. In the first series, polar (A1P to A5P) and semipolar (A1SP to A5SP) samples were grown simultaneously with the reactor pressure of 50 mbar, and growth temperature of 1100 °C. In the second series, only polar samples (B1P B5P) were grown at 50 mbar and 1115 °C. Finally, polar (C1P C5P) and semipolar (C1SP C5SP) samples were grown simultaneously at 200 mbar and 1100 °C. For each group of the samples V/III ratio and TMAl/(TMGa + TMAl) ratio are listed in table 1. These quite significantly different conditions resulted in variations between the series in terms of average compositions and growth rates; the latter were found to be about 0.23, 0.66 and 0.31 nm s^{-1} for series A, B and C, respectively. The thickness of the doped films in all experiments was kept within the range of 800–1100 nm. More details on the growth of polar samples in series A and B are also given in [28] and for semipolar samples in the series A in [29]. The AlN alloy fraction and the dopant concentration were determined using WDX measurements. Note that the AlN fractions quoted in [29] were measured by x-ray diffraction, which results in slight differences. Before the WDX examination,

all samples and composition standards (AlN, GaN and Si) were carbon-coated to reduce the effect of charging. WDX measurements were performed with an electron probe microanalyser (EPMA, JEOL JXA-8530F) at an acceleration voltage of 10 kV and a beam current of 40 nA. At these conditions, the interaction volume is kept within the first 800 nm of the $Al_xGa_{1-x}N$ layers according to Monte Carlo simulations using CASINO software [35]. For WDX point measurements quantitative data is an average of nine independent measurements selected away from larger 3D features across the sample surface. Any longer range compositional variations in the bulk film were below the detection limit of the WDX measurements. In the quantitative analysis x-ray line intensities emitted from the main specimens (L_α for Ga and K_α for Al, N, Si) were compared against the same x-ray line from the standard samples with known concentrations (AlN, GaN and Si). The measured intensities were then corrected for differences in composition between the standard and main specimens using an iterative procedure to give accurate atomic percentages of the species [36]. For estimating the Si concentration, a calibration method was used. The method involves measuring the Si intensity of all samples and comparing with $Al_xGa_{1-x}N$ and GaN reference samples for which Si concentration was known from secondary ion mass spectrometry (SIMS) analysis [37, 38]. Doping densities evaluated by this method are in the of range 10^{17}–10^{19} cm^{-3}. The concentration determined directly from the WDX are over-estimated, likely as a result of surface contamination [38].

The surface quality was examined using secondary electron (SE) imaging in a low-vacuum field emission gun scanning electron microscope (FEG-SEM, FEI Quanta 250 FEG). The morphology was also investigated using a Veeco multimode V atomic force microscope (AFM) in tapping mode. Images were also acquired in backscattered electron (BSE) mode, yielding compositional contrast dependent on the average atomic number of the material (Z).

CL spectra were recorded from uncoated samples in the low-vacuum FEG-SEM with a chamber pressure of 1 mbar, electron beam voltage of 15 kV and a beam current of 14 nA. Spectra were recorded with a spectral resolution of 0.8 nm, using a spectrometer with a 600 lines/mm grating blazed at 200 nm, a 50 μm slit, a focal length of 125 mm, and a 1600-element charge-coupled device. CL maps were recorded with the same spectrometer at 0.5 mbar chamber pressure [39]. The optical information obtained using CL was combined with the SE imaging to provide highly spatially resolved correlation of topography and optical properties [12].

3. Results and discussion

3.1. Surface morphology of the n-$Al_xGa_{1-x}N$ films

The surface morphology was examined by AFM for samples grown with different Si_2H_6 flow rates (1 and 3 sccm). The root mean square (RMS) roughness values were examined for 2 μm × 2 μm scan areas, giving average values of 4.35 and 3.76 nm for the polar and semipolar samples, respectively. The semipolar samples were found to have smoother surfaces than their polar counterparts, with an approximate 15% reduction in RMS. The surfaces of the semipolar samples are stable and not changed with different Si_2H_6 flow rates [40, 41].

Figure 1 shows BSE micrographs of representative n-$Al_xGa_{1-x}N$ films grown on AlN/sapphire. The surface of polar sample C4P reveals brighter regions around hexagon edges (figure 1(c)), which is indication of a locally lower AlN alloy fraction [12]. These are less clear in the lower AlN alloy fraction polar layer (A1P) shown in figure 1(a), but become apparent using the WDX mapping, which is discussed later. The surfaces of semipolar samples A4SP and C4SP reveal considerably fewer three-dimensional (3D) features (figures 1(b) and (d), respectively).

In general, due to the lattice mismatch between $Al_xGa_{1-x}N$ and the underlying AlN layer, the resulting compressive strain can be relaxed either through formation of additional dislocations (favored for $Al_xGa_{1-x}N$ with high x) or through enhanced surface roughening (preferable for low x) [42]. However in the case of n-$Al_xGa_{1-x}N$ with high doping levels (>10^{18} cm^{-3}) and typical crystal quality (total dislocation density ~10^9–10^{10} cm^{-2}), tensile strain gradually builds-up during the n-$Al_xGa_{1-x}N$ growth [43].

All the c-plane samples show hexagonal platelet structures and small hillock grains; additionally differently oriented crystallites are observed on their surfaces with no visible pits. The suppression of 3D nucleation for higher AlN alloy fraction c-plane samples is expected, due to the lower diffusion length of Ga adatoms at the higher TMAl flux necessary for their growth [44]. Also, compressive stress is reduced with increasing AlN alloy fraction in $Al_xGa_{1-x}N$/AlN and thus reduced defect formation is expected [42]. However, neither of the above effects are observed in our samples, as shown later in figures 5(c), (d) and (e).

There is no clear correlation between the diameter of the hexagonal platelets and the Si_2H_6 flow rate. The average hexagon diameter varies between 3.5 and 7 μm. Some similar samples have been assumed to be free from stress due to the occurrence of 3D growth [45] but in the present case the layers are smooth on a macroscopic scale and still under stress, as shown by x-ray diffraction measurements (not shown here). The polar layer deposited at a high V/III ratio of 600 (figure 1(a)) shows a rough surface morphology with some pyramidal hillocks of different sizes. On the other hand, the layer deposited at a lower V/III ratio of 23 (figure 1(c)) shows a similar morphology, but with similarly sized hexagons on the surface. For the c-plane samples in the B series, the surface morphology seems to be optimal with the intermediate V/III ratio of 460 (figure 1(e)). For the polar samples in the series C, there is a trend of increasing diameter of hexagonal platelets with increasing Si concentration. It may be possible that Si doping favors the stabilization and development of crystallographic facets [46]. There is no obvious correlation between Si concentration and the smoothness of surface morphology due to the enhanced mobility of the adatoms.

The set of semipolar samples (A and C) appears to have formed a continuous film, as seen in figures 1(b) and (d). For the same V/III ratio, their AlN fraction is lower compared to

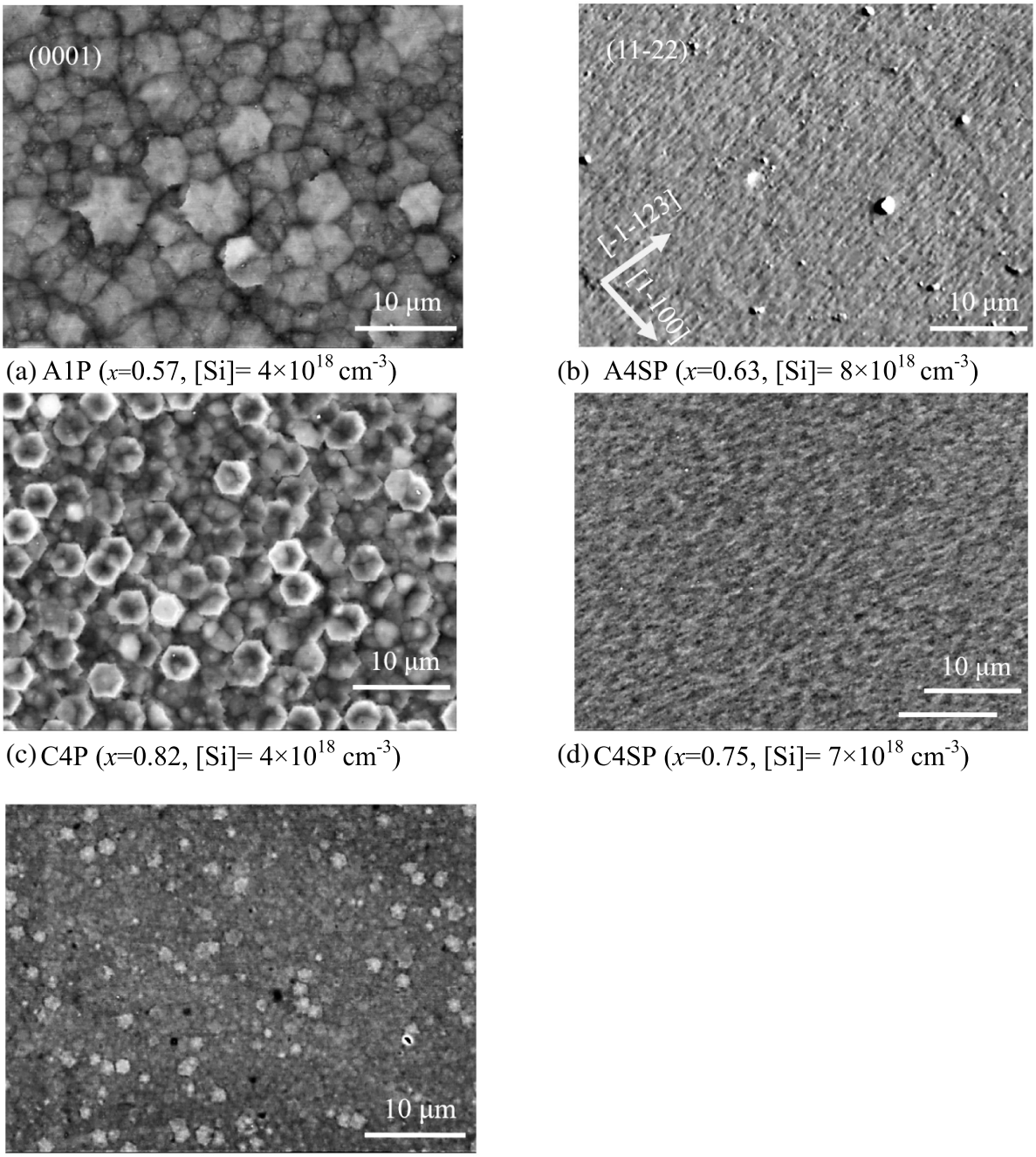

(a) A1P (x=0.57, [Si]= 4×10^{18} cm^{-3})

(b) A4SP (x=0.63, [Si]= 8×10^{18} cm^{-3})

(c) C4P (x=0.82, [Si]= 4×10^{18} cm^{-3})

(d) C4SP (x=0.75, [Si]= 7×10^{18} cm^{-3})

(e) B5P (x=0.84, [Si]= 5×10^{18} cm^{-3})

Figure 1. BSE micrographs of the $Al_xGa_{1-x}N$ layers with polar (left column) and semipolar (right column) orientations, details in table 1.

the polar samples grown at the same time, as shown in table 1. Some triangular, dot-like and small hillock-like features can be observed on the surface of the semipolar samples (figures 1(b) and (d)) [41]. The samples with the highest Si_2H_6 flow rate have the roughest surface (i.e. samples A4SP and A5SP).

3.2. WDX measurement

Table 1. presents the WDX measured compositions and doping levels for all the samples. Each of the reported values is the mean of nine measurements, chosen arbitrarily across the sample surface. The standard errors calculated for the AlN atomic fractions are 0.02–0.05, likely caused by compositional inhomogeneities on the samples, as they are too large to be purely caused by the technique limitations. The overall weight total for each of the samples investigated (the sum of mass percentages for all independently measured elements) was (100 ± 2) %, confirming a successful WDX analysis for the major elements.

Comparing the measured AlN alloy fraction for the samples within the same series but of different crystal orientations,

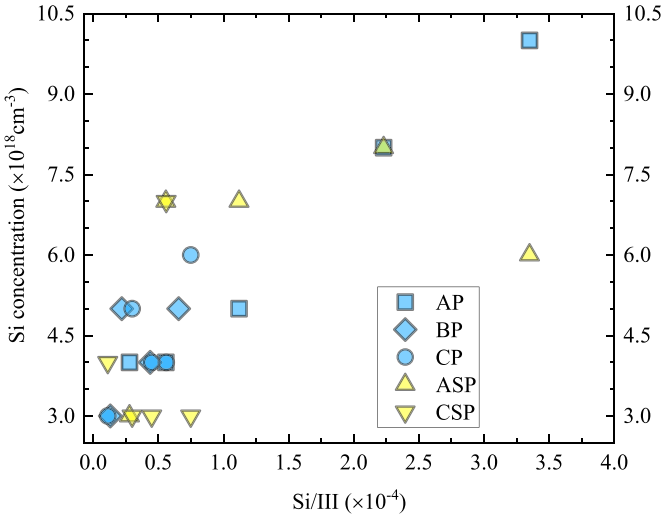

Figure 2. Si concentration of the n-$Al_xGa_{1-x}N$ layers as a function of Si_2H_6 to group-III ratio. The anomalous sample, B3P, has not been included in this plot.

one can see that AlN alloy fraction is lower in the semipolar samples, in agreement with [40], although there are reports of different relationships between AlN alloy fraction and orientation [41, 47]. For the samples with high V/III ratios, the AlN alloy fraction values are also lower due to increased TMAl:NH_3 pre-reactions and the suppression of GaN decomposition at increased ammonia fluxes [26, 48]. For example, for the semipolar samples in series A, grown with a V/III ratio of 600 and TMAl/(TMGa + TMAl) ratio of 0.5, the AlN alloy fraction is estimated to be 0.57–0.65 as compared with the samples in the series C, grown with the lower V/III ratio of 23 and TMAl/(TMGa + TMAl) ratio of 0.333, where it is estimated to be 0.75–0.78 (table 1).

Figure 2 shows the measured Si concentration of the n-$Al_xGa_{1-x}N$ layers as a function of Si_2H_6 to group-III ratio. There is a general trend of linearly increasing Si concentration with increasing Si/III ratio, although with a significant scattering of data. At a Si/III ratio above 2.3×10^{-4} a saturation of the Si concentration is observed for the semipolar samples in series A (ASP). The semipolar samples in series C (CSP) have lower Si/III ratios and although it is harder to be definitive about saturation, it is noted that the Si concentration drops for the highest Si/III ratio.

The saturation point is consistent with the work from Dinh *et al* [25], who used Hall data to show that the carrier concentration and mobility of the semipolar ASP layers reach a maximum at a similar Si/III ratio. The polar samples in series A (AP) exhibit an almost linear increase of [Si] with increasing Si_2H_6 flow rate, with no evidence of saturation. Interestingly, the trend is very different from the co-loaded semipolar samples (series ASP) with a much higher Si incorporation for A2SP (compared to A2P) followed by a saturation for A4SP. The polar samples in series B (BP) lie on a line parallel to the samples in series A, with the exception of B3P, which has a much higher Si incorporation. Hall-effect measurements for the polar samples in series B show a monotonic decrease of the Hall coefficient with increasing Si_2H_6 flow rate [26], strongly indicating that sample B3P is anomalous. For the polar samples in series C (CP), [Si] seems to lie roughly on the same line as the A and B sets. The polar C series shows an approximate linear increase with Si/III ratio. However, the Si/III ratios do not extend above 0.75×10^{-4} in both C series and the [Si] measurements for the semipolar CSP samples show significant scatter.

3.3. WDX mapping

According to Mogilatenko *et al* [42], the difference in AlN fraction of the $Al_xGa_{1-x}N$ regions on planar c-plane terraces and on the side facets of the surface macrosteps corresponds to at least 0.1 (10% AlN fraction) for $x = 0.6$ and around 0.04 (4% AlN fraction) for $x = 0.8$.

Due to difference in surface mobility between Al and Ga adatoms the lowest Ga incorporation happens on the top facets of the hexagons [45], while Al adatoms are readily incorporated onto any $Al_xGa_{1-x}N$ surface due to their lower surface diffusion length [49]. Ga adatoms have a longer diffusion length increasing the chance of incorporating at an energetically more favorable site or being irreversibly desorbed to the ambient. From our observations, it is clear that with hexagonal features in sample C1P, Ga will be trapped around the feature edges, resulting in an increased Ga incorporation. However, on the feature top surfaces, effective areas are larger and smoother, leading to a faster Ga diffusion. That is one of the reasons why a GaN-rich phase is noticeable at the boundaries of 3D surface features [45, 50]. A possible explanation for this observation is that island boundaries provide additional chemical bonds where Ga can be retained, resulting in Ga accumulation [50].

The experimental data for the polar sample C1P in figure 3 show a higher (lower) intensity of Ga L_α (Al K_α) x-rays around the hexagon edges; the same behavior is observed in the compositional BSE image. Comparing these maps allows us to rule out topographic effects as the dominant source of contrast, in which an increased backscatter signal would result in fewer x-ray counts. Seeing bright edges in both therefore unambiguously points to higher mass regions in a way that either map alone would not. Despite the challenging signal-to-noise ratio, inherent to x-ray counting statistics, we can see clear variations in the Ga distribution on a sub-μm length scale. The GaN alloy fraction was quantified using the measured GaN at% from WDX quantitative point data giving an estimate of 18% GaN at the middle of the map (figure 3(b)). The observed difference from center to edge of a hexagon is about 2% GaN. In contrast, a WDX map of a semipolar sample (A5SP), whose surface is free from hexagons, does not reveal any observable variation between Ga L_α and Al K_α x-rays (therefore not presented), indicating better compositional homogeneity compared to polar samples.

3.4. CL mapping

CL hyperspectral mapping enables us to correlate optical properties with surface morphology by mapping variations in

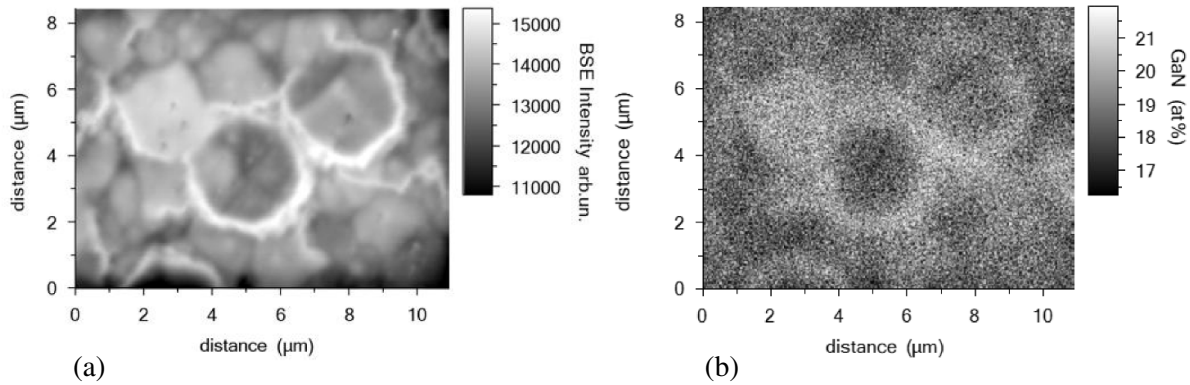

Figure 3. Composition mapping of the *c*-plane sample C1P (81% AlN mole fraction). (a) BSE image of the measured area, (b) GaN content map (at%) obtained from a WDX map of the Ga L_α x-ray intensity.

spectral luminescence across a sample [51, 52]. The acquired CL images can be simultaneously or sequentially (as in this work) correlated with WDX spot analyses or maps, thus enabling specific CL characteristics to be related to semiconductor composition [52].

CL spectra were measured for all samples, and maps collected for selected polar samples. The spectra revealed near-band edge (NBE) peaks in the photon energy range of 4.0–5.4 eV and impurity transition peaks in the range of 2.7–4.8 eV. An example of a typical CL spectrum is shown in (figure 4(b)), for the sample C1P.

The impurity transitions are assigned to recombination between shallow donors and deep level acceptors including cation vacancies $(V_{III})^{3-}$ and V_{III} complexes (e.g. $(V_{III}{}^{-}O)^{2-}$) [53].

One of the explanations for the introduction of the vacancy type defects is related to the transition of the growth mode from 2D growth to 3D growth [14]. Cation vacancies act as non-radiative recombination centers in $Al_xGa_{1-x}N$, and it is possible that they are introduced by Si doping due to a decrease in their formation energy as the Fermi level moves towards the conduction band [20].

The CL intensity maps (figures 4(c)–(f)), extracted from the hyperspectral data set, reveal domains between which there are shifts in the $Al_xGa_{1-x}N$ NBE emission energy. The 2D CL intensity maps were extracted from the 3D data cube by integrating over a given spectral window, while calculating a centroid over the same range generates a map of emission energy [54].

Regions of higher CL intensity in the NBE peak intensity map (figure 4(c)) correlate with lower emission energy in the corresponding NBE energy map (figure 4(d)), following the same trend as compositional variations revealed by the WDX mapping (figure 3(b)). While these alloy variations are likely the dominant cause of the observed peak shift, additional contributions from non-uniform elastic strain and carrier concentrations cannot be discounted.

Figure 4(c) reveals an increase in the NBE intensity all the way along the edges of the hexagons compared to the middle of the feature. The intensity map of the $(V_{III}$ complex$)^{1-}$ defect peak, figure 4(e), seems to be more localized and higher intensity spots are observable along the edges of the hexagon. Oxygen can possibly be more easily incorporated at the semipolar facets of the hexagons [12].

For the other two defect peaks ($(V_{III}$ complex$)^{2-}$ and $(V_{cation})^{3-}$) a higher intensity is measured from the middle of hexagon, figure 4(f), which contrasts with the behavior of the other peaks. A screw dislocation has been reported to emerge at the middle of the hexagon [12], with which the defect complex $(V_{cation})^{3-}$ could be related, additionally we found that the AlN composition is higher in the middle of the hexagons which could lead to a locally lower formation energy of these defects.

At the edges of the hexagon, the growth conditions differ from the rest of the sample, as discussed above. In the case of the *c*-plane sample C1P (81% AlN), the hexagon center shows 98% of the mean whole map intensity and the edge 101%.

For sample A1P (63% AlN), the difference in NBE intensity from different parts of the sample is larger (the center of hexagon shows 95% of the mean map intensity and the edge 109%). Also, the shift in the NBE emission energy from center to edge is found to be larger in this case of 110 meV compared to 60 meV for C1P (figure 4(d)). The CL map of sample A1P not presented as it demonstrates exactly the same type of luminescence behavior as seen in sample C1P. This shift for sample C1P corresponds to a difference of about 1.5% in GaN content, which compares well with the 2 at% GaN difference estimated from the WDX map. From these observations, it is apparent that the sample grown with the highest V/III ratio of 600 and with $x < 0.63$ (A1P) shows higher compositional inhomogeneity compared to the sample grown at lower V/III ratio of 23 and with $x > 0.81$ (C1P).

3.5. CL spectra

Figure 5 shows mean CL spectra for all *c*-plane and semipolar sample series. It is noticeable that the intensities of the deep impurity transitions are on the same order or higher than those of the band-edge transitions. Each set of CL spectra (figures 5(a)–(e)) represents samples with a particular V/III ratio and orientation, and shows how the relative intensity of the NBE peaks and impurity transitions, depend strongly

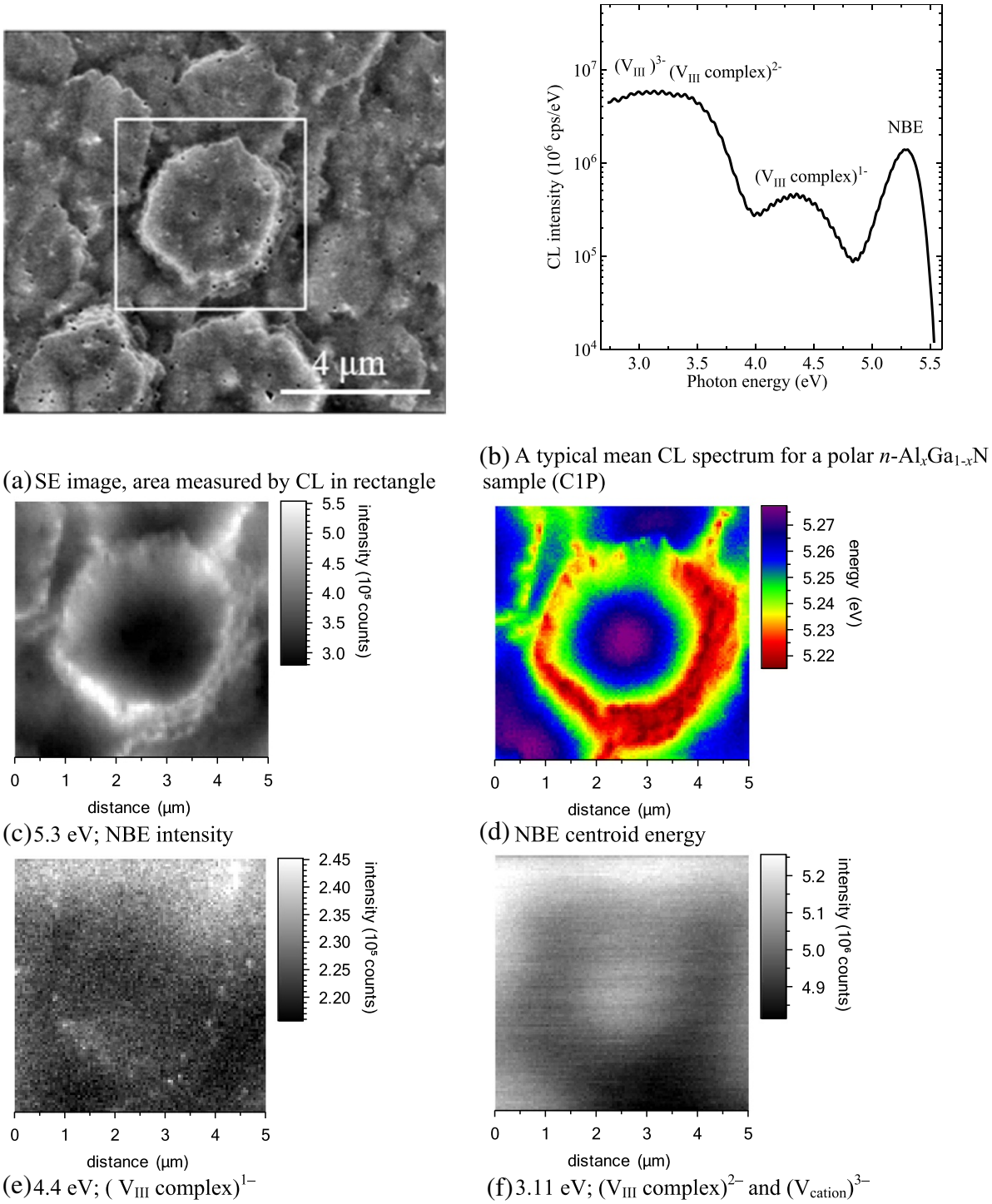

Figure 4. CL imaging of the *c*-plane C1P sample: including SE image (a), mean CL spectrum (b) and 5 × 5 μm^2 CL maps of the sample (c)-(f).

on the growth conditions. Similar behavior was reported in [12, 25]. Figure 6 plots the peak wavelengths of the impurity transitions observed in the spectra as a function of AlN content, alongside previously published data [29], in order to clarify the origins of the peaks.

The spectra in figures 5(a), (b) and (e) (which correspond to the polar and semipolar samples in the series A, and polar samples in the series C, respectively) reveal $(V_{III})^{3-}$, $(V_{III}\ complex)^{2-}$, $(V_{III}\ complex)^{1-}$ impurity peaks and NBE peaks. For the polar samples in the series A, the intensity of the NBE peak increases with Si content, as well as the intensity of the $(V_{III}\ complex)^{1-}$ peak for A1P–A4P samples. $(V_{III}\ complex)^{1-}$ peak decreases again for A5P where the $(V_{III}\ complex)^{2-}$ becomes strongest. The $(V_{III}\ complex)^{2-}$ peak becomes visible in higher Si content samples (A3P–A5P) and follows the same trend, with the intensity of the peak

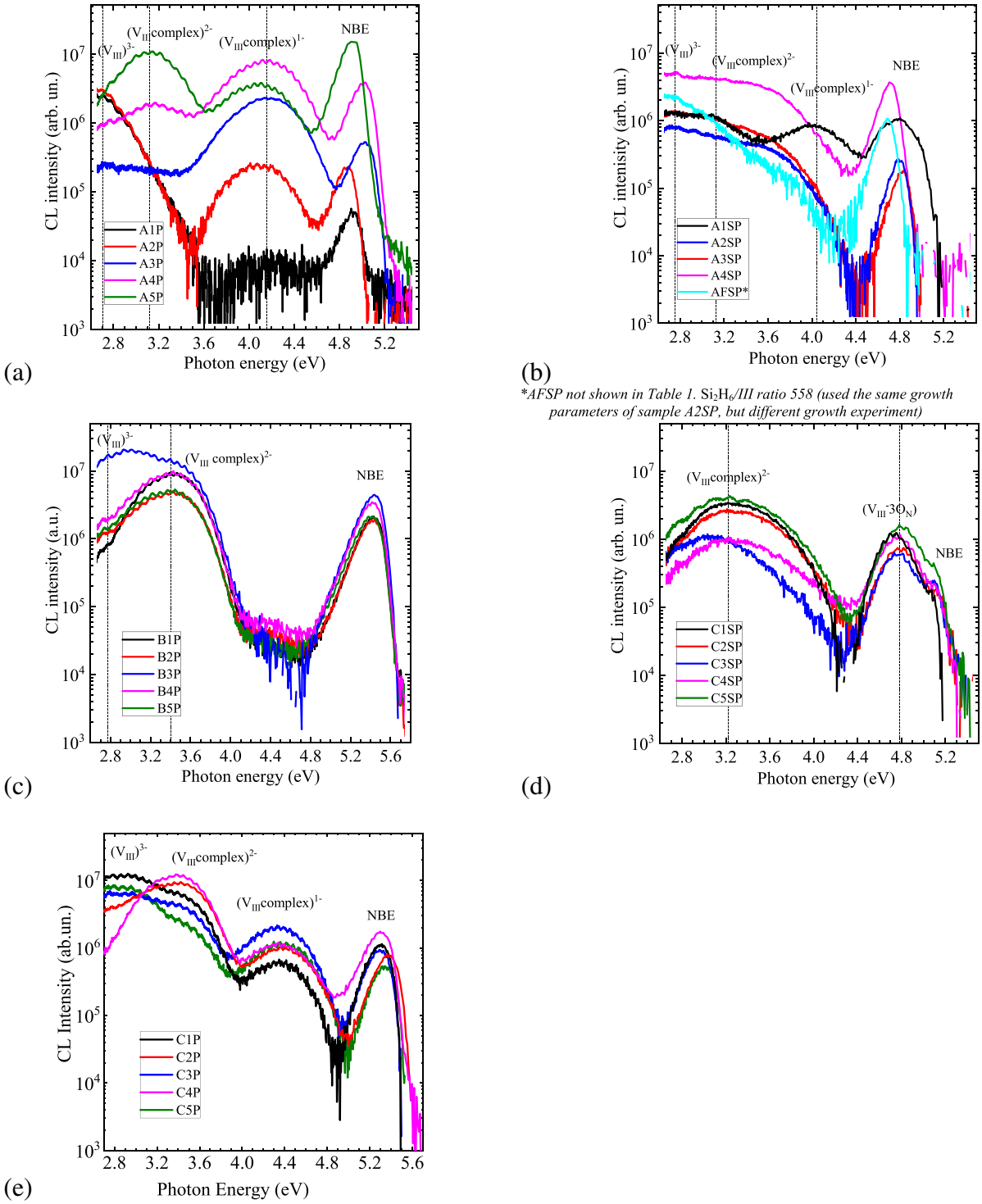

Figure 5. Room temperature (300 K) CL spectra of n-$Al_xGa_{1-x}N$ layers: (a) c-plane layers (series A), $x = 0.63$–0.72, (b) semipolar layers (series A), $x = 0.57$–0.65, (c) c-plane layers (series B), $x = 0.84$–0.85, (d) semipolar layers (series C), $x = 0.75$–0.78, (e) c-plane layers (series C), $x = 0.81$–0.82.

increasing with Si content. The $(V_{III})^{3-}$ intensity is highest for lowest Si content samples (A1P and A2P). As described earlier, WDX and Hall data indicate that the Si incorporation saturated in the semipolar ASP series and it is notable that the $(V_{III}\ complex)^{1-}$ and $(V_{III}\ complex)^{2-}$ peaks are hardly present in the CL spectra from the more highly doped samples in this series. This may be related to a low solubility limit for Si in the semipolar samples, although further research is needed to confirm this.

For the polar samples in series C, the intensity of the NBE decreases with increasing [Si], as well as the intensity of the $(V_{III}\ complex)^{2-}$ peak as seen in figure 5(e).

For the polar samples in the series B and the semipolar samples in the series C the $(V_{III}\ complex)^{1-}$ is not

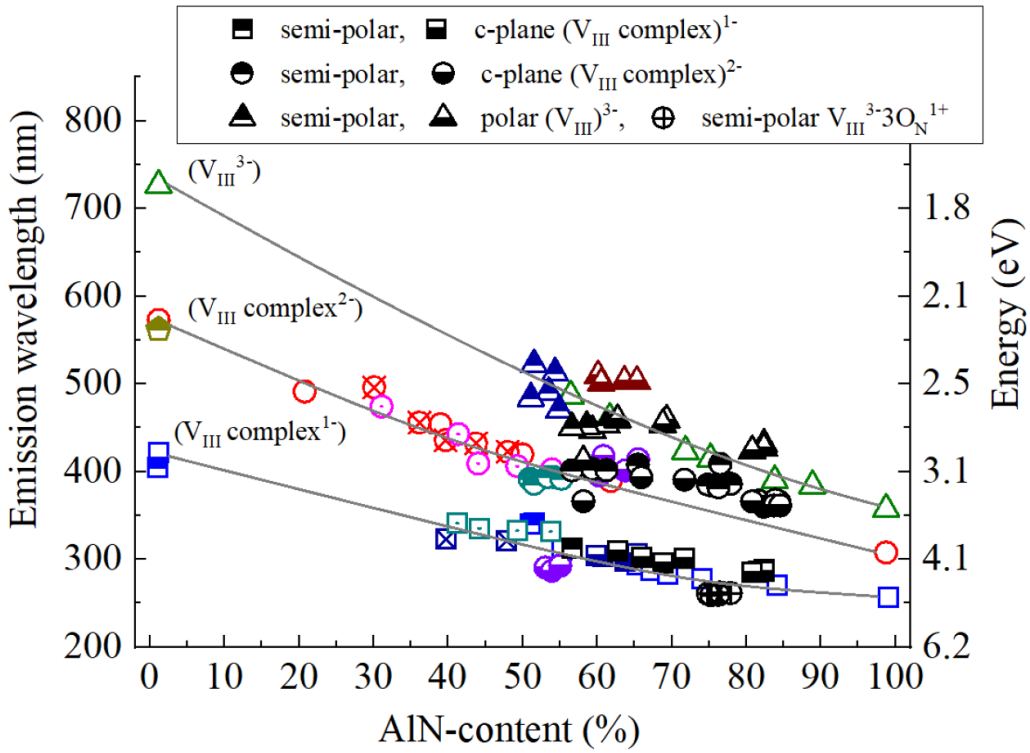

Figure 6. CL peak positions of deep impurity transitions obtained from figure 5 as a function of AlN-alloy fraction. The results from this work (black and white symbols) are plotted against previously published data (colored symbols) from [29] for comparison. The solid lines provide guides to the eye.

present, as shown in figures 5(c) and (d). The V_{III} complex with oxygen is only visible in figure 5(d) for the semipolar samples in the series C. Oxygen can behave as an electron acceptor in $Al_xGa_{1-x}N$ and hinder *n*-type behavior achieved with Si doping, similar to cation vacancies [19, 20, 55]. The aforementioned complex could be associated also with N vacancies, since the growth was performed at very low V/III ratio of 23 [48].

4. Conclusion

The compositional and optical properties of semipolar (11–22) and polar (0001) *n*-$Al_xGa_{1-x}N$ films have been systematically investigated using WDX and CL measurements. The Si-doping concentration was measured by WDX, using calibration data from SIMS.

Comparison of the measured AlN alloy fraction for samples with different crystal orientations showed that the AlN incorporation was higher in the polar samples. The highest values of Si incorporations were observed for the polar samples with the highest Si/III ratios, while saturation of Si incorporation was seen for the semipolar samples at higher Si/III ratios.

CL hyperspectral imaging of the polar samples revealed significant reductions in NBE luminescence intensity from the middle of surface hexagonal features where a threading dislocation is expected to be terminated. WDX mapping confirmed higher Ga incorporation around the hexagon edges. The semipolar samples showed no such features, corresponding to a better compositional homogeneity. CL point spectra showed how changes in the relative intensity of the NBE peaks and impurity transitions depend strongly on the growth conditions and surface orientations.

The main implication of this work for LED research is the use of the CL technique to identify the suppression of impurity defects, which will lead to further improvements in the layer conductivity since they act as recombination centers. The analysis of CL data can therefore help reduce point defect densities by guiding the optimization of growth parameters. The technique is potentially also informative for other layers grown under similar conditions where point defects cannot be directly measured, such as quantum wells. The CL and WDX results presented in this paper provide information on how point defect incorporation in the doped AlGaN contact layers is influenced by crystal orientation, alloy composition, and Si incorporation, as well as on the existence of different compensating defects. This paper also highlights challenges associated with growth of high AlN content AlGaN layers such as occurrence of hexagonal platelet structures in *c*-plane samples and compositional inhomogeneity.

Acknowledgments

This work was supported by the EPSRC project EP/N010914/1, 'Nanoanalysis for Advanced Materials and Healthcare', by the EU-FP7 programme 'ALIGHT', Science Foundation Ireland through SFI/10/IN.1/I2993 and Irish Photonic Integration Centre (SFI/12/RC/2276_2); and the European Space Agency.

Data availability

The datasets that support the findings of this study can be found online under DOI: 10.15129/d7c54205-9bca-4785-9b3e-1e6a2b182771.

ORCID iDs

Lucia Spasevski
https://orcid.org/0000-0002-7409-3807
Gunnar Kusch
https://orcid.org/0000-0003-2743-1022
Pietro Pampili
https://orcid.org/0000-0003-4163-4475
Vitaly Z Zubialevich
https://orcid.org/0000-0003-4783-5104
Duc V Dinh
https://orcid.org/0000-0002-5915-3365
Jochen Bruckbauer
https://orcid.org/0000-0001-9236-9320
Paul R Edwards
https://orcid.org/0000-0001-7671-7698
Peter J Parbrook
https://orcid.org/0000-0003-3287-512X
Robert W Martin
https://orcid.org/0000-0002-6119-764X

References

[1] Kneissl M *et al* 2011 Advances in group III-nitride-based deep UV light-emitting diode technology *Semicond. Sci. Technol.* **26** 014036
[2] Ding K, Avrutin V, Özgür Ü and Morkoç H 2017 Status of growth of group III-nitride heterostructures for deep ultraviolet light-emitting diodes *Crystals* **7** 300
[3] Kneissl M, Seong T-Y, Han J and Amano H 2019 The emergence and prospects of deep-ultraviolet light-emitting diode technologies *Nat. Photon.* **13** 233
[4] Yu E T, Dang X Z, Asbeck P M, Lau S S and Sullivan G J 1999 Spontaneous and piezoelectric polarization effects in III–V nitride heterostructures *J. Vac. Sci. Technol.* B **17** 1742
[5] Hakamata J, Kawase Y, Dong L, Iwayama S, Iwaya M, Takeuchi T, Kamiyama S, Miyake H and Akasaki I 2018 Growth of high-quality AlN and AlGaN films on sputtered AlN/sapphire templates via high-temperature annealing *Phys. Status Solidi* b **255**
[6] Cho H K, Lee J Y, Jeon S R and Yang G M 2001 Structural properties of Si and Mg doped and undoped Al0.13Ga0.87N layers grown by metalorganic chemical vapor deposition *J. Cryst. Growth* **233** 667
[7] Inoue S-I, Tamari N and Taniguchi M 2017 150 mW deep-ultraviolet light-emitting diodes with large-area AlN nanophotonic light-extraction structure emitting at 265 nm *Appl. Phys. Lett.* **110** 141106
[8] Kaneda M, Pernot C, Nagasawa Y, Hirano A, Ippommatsu M, Honda Y, Amano H and Akasaki I 2017 Uneven AlGaN multiple quantum well for deep-ultraviolet LEDs grown on macrosteps and impact on electroluminescence spectral output *Japan. J. Appl. Phys.* **56** 061002
[9] Zhu K, Nakarmi M L, Kim K H, Lin J Y and Jiang H X 2004 Silicon doping dependence of highly conductive n-type Al0.7Ga0.3N *Appl. Phys. Lett.* **85** 4669
[10] Pampili P and Parbrook P J 2017 Doping of III-nitride materials *Mater. Sci. Semicond. Process.* **62** 180
[11] Taniyasu Y, Kasu M and Kobayashi N 2002 Intentional control of n-type conduction for Si-doped AlN and AlXGa1−XN (0.42⩽x<1) *Appl. Phys. Lett.* **81** 1255
[12] Kusch G *et al* 2015 Spatial clustering of defect luminescence centers in Si-doped low resistivity Al0.82Ga0.18N *Appl. Phys. Lett.* **107** 072103
[13] Kurai S, Ushijima F, Miyake H, Hiramatsu K and Yamada Y 2014 Inhomogeneous distribution of defect-related emission in Si-doped AlGaN epitaxial layers with different Al content and Si concentration *J. Appl. Phys.* **115** 053509
[14] Uedono A, Tenjinbayashi K, Tsutsui T, Shimahara Y, Miyake H, Hiramatsu K, Oshima N, Suzuki R and and Ishibashi S 2012 Native cation vacancies in Si-doped AlGaN studied by monoenergetic positron beams *J. Appl. Phys.* **111** 013512
[15] Murotani H, Yamada Y, Miyake H and Hiramatsu K 2011 Silicon concentration dependence of optical polarization in AlGaN epitaxial layers *Appl. Phys. Lett.* **98** 021910
[16] Cantu P, Wu F, Waltereit P, Keller S, Romanov A E, Mishra U K, DenBaars S P and Speck J S 2003 Si doping effect on strain reduction in compressively strained Al0.49Ga0.51N thin films *Appl. Phys. Lett.* **83** 674
[17] Mehnke F, Trinh X T, Pingel H, Wernicke T, Janzén E, Son N T and Kneissl M 2016 Electronic properties of Si-doped Alx Ga1−xN with aluminum mole fractions above 80% *J. Appl. Phys.* **120** 145702
[18] Harris J S, Gaddy B E, Collazo R, Sitar Z and Irving D L 2019 Oxygen and silicon point defects in Al0.65Ga0.35N *Phys. Rev. Mater.* **3**
[19] Thonke K, Lamprecht M, Collazo R and Sitar Z 2017 Optical signatures of silicon and oxygen related DX centers in AlN *Phys. Status Solidi* a **214** e201600749
[20] Stampfl C and Walle C G V D 1998 Doping of AlxGa1−xN *Appl. Phys. Lett.* **72** 459
[21] Amano H *et al* 2020 The 2020 UV emitter roadmap *J. Phys. D: Appl. Phys.* **53** 503001
[22] Bryan Z *et al* 2014 Fermi level control of compensating point defects during metalorganic chemical vapor deposition growth of Si-doped AlGaN *Appl. Phys. Lett.* **105** 222101
[23] Mehnke F *et al* 2013 Highly conductive n-AlxGa1−xN layers with aluminum mole fractions above 80% *Appl. Phys. Lett.* **103** 212109
[24] Nakarmi M L, Kim K H, Zhu K, Lin J Y and Jiang H X 2004 Transport properties of highly conductive n-type Al-rich AlxGa1−xN(x⩾0.7) *Appl. Phys. Lett.* **85** 3769
[25] Dinh D V, Pampili P and Parbrook P J 2016 Silicon doping of semipolar (112¯2)AlxGa1−xN(0.50≤x≤0.55) *J. Cryst. Growth* **451** 181
[26] Pampili P, Dinh D V, Zubialevich V Z and Parbrook P J 2018 Significant contribution from impurity-band transport to the room temperature conductivity of silicon-doped AlGaN *J. Phys. D: Appl. Phys.* **51** 06LT01
[27] Jo M, Oshima I, Matsumoto T, Maeda N, Kamata N and Hirayama H 2017 Structural and electrical properties of semipolar (11-22) AlGaN grown on m-plane (1-100) sapphire substrates *Phys. Status Solidi* c **14** 1600248
[28] Nepal N, Li J, Nakarmi M L, Lin J Y and Jiang H X 2006 Exciton localization in AlGaN alloys *Appl. Phys. Lett.* **88** 062103
[29] Bryan Z, Bryan I, Xie J, Mita S, Sitar Z and Collazo R 2015 High internal quantum efficiency in AlGaN multiple quantum wells grown on bulk AlN substrates *Appl. Phys. Lett.* **106** 142107
[30] Li Z, Wang L, Jiu L, Bruckbauer J, Gong Y, Zhang Y, Bai J, Martin R W and Wang T 2017 Optical investigation of semi-polar (11-22) AlxGa1-xN with high Al composition *Appl. Phys. Lett.* **110** 091102
[31] Huakai L, Xiong Z, Zongwen L, Yi W, Qian D, Hongquan Y, Zili W, Jianguo Z and Yiping C 2017 Epitaxial growth of

semi-polar (11-22) plane AlGaN epi-layers on m-plane (10-10) sapphire substrates *Phys. Status Solidi* a **214** 1600802
[32] Dridi Z, Bouhafs B and Ruterana P 2003 First-principles investigation of lattice constants and bowing parameters in wurtzite AlxGa1xN, InxGa1xN and InxAl1xN alloys *Semicond. Sci. Technol.* **18** 850
[33] Li H, Sadler T C and Parbrook P J 2013 AlN heteroepitaxy on sapphire by metalorganic vapour phase epitaxy using low temperature nucleation layers *J. Cryst. Growth* **383** 72
[34] Dinh D V, Conroy M, Zubialevich V Z, Petkov N, Holmes J D and Parbrook P J 2015 Single phase (112¯2) AlN grown on (101¯0) sapphire by metalorganic vapour phase epitaxy *J. Cryst. Growth* **414** 94
[35] Drouin D, Couture A R, Joly D, Tastet X, Aimez V and Gauvin R 2007 CASINO V2.42—A fast and easy-to-use modeling tool for scanning electron microscopy and microanalysis users *Scanning* **29** 92
[36] Kusch G, Mehnke F, Enslin J, Edwards P R, Wernicke T, Kneissl M and Martin R W 2017 Analysis of doping concentration and composition in wide bandgap AlGaN:Si by wavelength dispersive x-ray spectroscopy *Semicond. Sci. Technol.* **32** 035020
[37] Trager-Cowan C *et al* 2019 Scanning electron microscopy as a flexible technique for investigating the properties of UV-emitting nitride semiconductor thin films *Photon. Res.* **7** B73
[38] Spasevski L, Buse B, Enslin J, Wernicke T, Mehnke F, Kneissl M, Edwards P R and Martin R W 2020 New approach for studying silicon doping in AlGaN films by wavelength-dispersive x-ray microanalysis in preparation
[39] Edwards P R and Martin R W 2011 Cathodoluminescence nano-characterization of semiconductors *Semicond. Sci. Technol.* **26** 064005
[40] Dinh D V, Alam S N and Parbrook P J 2016 Effect of V/III ratio on the growth of (11 2¯ 2) AlGaN by metalorganic vapour phase epitaxy *J. Cryst. Growth* **435** 12
[41] Stellmach J, Mehnke F, Frentrup M, Reich C, Schlegel J, Pristovsek M, Wernicke T and Kneissl M 2013 Structural and optical properties of semipolar (112¯2) AlGaN grown on (101¯0) sapphire by metal–organic vapor phase epitaxy *J. Cryst. Growth* **367** 42
[42] Mogilatenko A, Küller V, Knauer A, Jeschke J, Zeimer U, Weyers M and Tränkle G 2014 Defect analysis in AlGaN layers on AlN templates obtained by epitaxial lateral overgrowth *J. Cryst. Growth* **402** 222
[43] Forghani K, Schade L, Schwarz U T, Lipski F, Klein O, Kaiser U and Scholz F 2012 Strain and defects in Si-doped (Al)GaN epitaxial layers *J. Appl. Phys.* **112** 093102
[44] Zeimer U, Kueller V, Knauer A, Mogilatenko A, Weyers M and Kneissl M 2013 High quality AlGaN grown on ELO AlN/sapphire templates *J. Cryst. Growth* **377** 32
[45] Kusch G, Li H, Edwards P R, Bruckbauer J, Sadler T C, Parbrook P J and Martin R W 2014 Influence of substrate miscut angle on surface morphology and luminescence properties of AlGaN *Appl. Phys. Lett.* **104** 092114
[46] Nilsson D, Janzén E and Kakanakova-Georgieva A 2014 Strain and morphology compliance during the intentional doping of high-Al-content AlGaN layers *Appl. Phys. Lett.* **105** 082106
[47] Dinh D V, Hu N, Honda Y, Amano H and Pristovsek M 2019 Aluminium incorporation in polar, semi- and non-polar AlGaN layers: a comparative study of x-ray diffraction and optical properties *Sci. Rep.* **9** 15802
[48] Dinh D V, Hu N, Honda Y, Amano H and Pristovsek M 2020 Pulsed-flow growth of polar, semipolar and nonpolar AlGaN *J. Mater. Chem.* C (https://doi.org/10.1039/D0TC01369B)
[49] Heying B, Tarsa E J, Elsass C R, Fini P, DenBaars S P and Speck J S 1999 Dislocation mediated surface morphology of GaN *J. Appl. Phys.* **85** 6470
[50] Mayboroda I O, Knizhnik A A, Grishchenko Y V, Ezubchenko I S, Zanaveskin M L, Kondratev O A, Presniakov M Y, Potapkin B V and Ilyin V A 2017 Growth of AlGaN under the conditions of significant gallium evaporation: phase separation and enhanced lateral growth *J. Appl. Phys.* **122** 105305
[51] Martin R W, Edwards P R, O'Donnell K P, Dawson M D, Jeon C-W, Liu C, Rice G R and Watson I M 2004 Cathodoluminescence spectral mapping of III-nitride structures *Phys. Status Solidi* a **201** 665
[52] Edwards P R, Naresh-Kumar G, Kusch G, Bruckbauer J, Spasevski L, Brasser C G, Wallace M J, Trager-Cowan C and Martin R W 2018 You do what in your microprobe?! The EPMA as a multimode platform for nitride semiconductor characterization *Microsc. Microanal.* **24** 2026
[53] Nepal N, Nakarmi M L, Lin J Y and Jiang H X 2006 Photoluminescence studies of impurity transitions in AlGaN alloys *Appl. Phys. Lett.* **89** 092107
[54] Edwards P R, Jagadamma L K, Bruckbauer J, Liu C, Shields P, Allsopp D, Wang T and Martin R W 2012 High-resolution cathodoluminescence hyperspectral imaging of nitride nanostructures *Microsc. Microanal.* **18** 1212
[55] Van de Walle C G, Stampfl C, Neugebauer J, McCluskey M D and Johnson N M 1999 Doping of AlGaN alloys *MRS Internet J. Nitride Semicond. Res.* **4** 890